ADVANCED MATERIALS
www.advmat.de

Dual Modification of Metal–Organic Frameworks for Exceptional High Piezo-Photocatalytic Hydrogen Production

Haijun Hu, Xiaoning Li, Kailai Zhang, Ge Yan, Weixiang Kong, Anqi Qin, Yali Ma, Aisen Li, Kai Wang, Hongwei Huang, Xiaodong Sun, and Tianyi Ma**

Metal–organic frameworks (MOFs) face significant challenges in photocatalysis due to severe carrier recombination. Here, a novel approach is presented that incorporates —NH_2 groups and Cu ions onto MOFs with a MIL-125 skeleton, forming NH_2-MIL-125 and Cu-NH_2-MIL-125. This modification effectively enhances the polarity of MOFs, evidenced by significantly increased d_{33} values (from 1.69 to 26.21 pm/V) and notable higher dipole moments (from 6.60 to 25.99 D). Notably, it's the first demonstration of boosting MOFs piezoelectricity via a dual modulation strategy. Moreover, the polarity can be further amplified by ultrasonic vibration based on the positive piezoelectric effect, which is justified by in situ Raman spectra, COMSOL simulations, and DFT calculations, by taking into account the applied pressure. The positive impact of introduced piezoelectric effect in facilitating charge separation and transfer of Cu-NH_2-MIL-125, proved by enhanced current response. Consequently, through coupling piezocatalysis and photocatalysis, the H_2 production rate of Cu-NH_2-MIL-125 can be significantly enhanced to ≈2884.2 μmol·g^{-1}·h^{-1}, 2.76 and 9.92 times higher than that of NH_2-MIL-125 and MIL-125, respectively, ranking first in all reported MOF-based piezo-photocatalysts. This research demonstrates the prospective opportunity for alleviating the severe carriers recombination problem for MOFs through the implantation of piezoelectric field driving force.

1. Introduction

Photocatalytic hydrogen evolution is an ideal technology for clean energy production, as it has potential to utilize abundant sunlight and water. However, most current catalysts fall short of meeting the demands for real-world applications, highlighting the urgent need of developing efficient photocatalysts.[1] Metal–organic frameworks (MOFs), a class of crystalline porous inorganic-organic material with high specific surface area, tuneable pore sizes, and tailored structure, has attracted extensive interest in the fields of gas adsorption, separation and storage, and drug delivery.[2–4] In recent years, MOFs materials have also emerged as star materials in the field of photocatalysis,[5] with unparalleled advantages in comparison with traditional semiconductor photocatalysts. First, the unique porosity and large specific surface area provide abundant surface reactive sites and allow for the incorporation of various photoactive materials within

H. Hu, K. Zhang, G. Yan, W. Kong, A. Qin, X. Sun
Institute of Clean Energy Chemistry
Key Laboratory for Green Synthesis and Preparative Chemistry of Adv. Mater.
College of Chemistry
Liaoning University
Shenyang 110036, P. R. China
E-mail: sunxiaodong@lnu.edu.cn

H. Hu, X. Li, T. Ma
Centre for Atomaterials and Nanomanufacturing (CAN)
School of Science
RMIT University
Melbourne, VIC 3000, Australia
E-mail: tianyi.ma@rmit.edu.au

The ORCID identification number(s) for the author(s) of this article can be found under https://doi.org/10.1002/adma.202419023

DOI: 10.1002/adma.202419023

X. Li, T. Ma
ARC Industrial Transformation Research Hub for Intelligent Energy Efficiency in Future Protected Cropping (E2Crop)
Melbourne, VIC 3000, Australia

Y. Ma
College of Chemical Engineering
Shenyang University of Chemical Technology
Shenyang 110142, P. R. China

A. Li, K. Wang
School of Physical Science and Information Technology
Liaocheng University
Liaocheng 252000, P. R. China

H. Huang
Beijing Key Laboratory of Materials Utilization of Nonmetallic Minerals and Solid Wastes
National Laboratory of Mineral Materials
School of Materials Science and Technology
China University of Geosciences
Beijing 100083, P. R. China

their pores and cages to facilitate the hydrogen generation reaction. Second, the periodic lattice structures effectively decrease the transfer distance of charges generated by light, which is beneficial for promoting photocatalytic reactions. Third, the structure can be easily modified by altering the substituents of the linker or by exchanging or doping the metal ions in the framework nodes, enabling straightforward manipulation of their band structure.[6–12] However, the photocatalytic activity of pure MOFs materials remains unsatisfactory due to the recombination of electron-hole pairs, which occurs within a few picoseconds, faster than the time required for charge carriers to migrate and react.[13] Therefore, improving the separation efficiency of photogenerated carriers in the bulk phase of MOFs materials is the key to put forward their applications for real-world hydrogen production. In order to address above issues, researchers have proposed various strategies, including metal doping, ligand functionalization, defect engineering, heterojunction construction, etc.[14–17] However, these methods have limitations in significantly enhancing the photocatalytic performance of MOFs-based materials, and the problem of bulk-phase charge recombination remains unresolved. Therefore, it is of great significance to provide a strong and persistent driving force for carrier separation within MOFs, which is necessary for continuously improving their photocatalytic efficiency.

In recent years, researchers have become convinced that enhancing the polarity of photocatalysts, by integrating piezoelectric catalytic technology with photocatalysis, can fundamentally improve their charge carriers separation.[18–23] The polarity of photocatalysts, which refers to their ability to develop distinct positive and negative charges, is closely linked to their piezoelectricity.[24–26] Based on the positive piezoelectric effect, positive and negative charges will be generated at both ends of the polar photocatalysts, forming a built-in piezoelectric field when applying an external force. Then, the electron-hole pairs generated by solar energy can be effectively separated under the effect of this built-in piezoelectric field. This necessitates that the photocatalysts possess notable piezoelectric properties.[27,28] Nevertheless, most of the reported MOFs own high symmetry and low polarity, leading to weak piezoelectric response signals are weak.

In this context, Zhang and co-workers improved the piezoelectric properties of MOFs through a polar metal center replacement strategy.[29] The two MOFs, UiO-66-NH_2(Zr) and UiO-66-NH_2(Hf), which have similar structures but different Zr/Hf-oxo clusters, exhibits distinct piezoelectric characteristics due to the varying polarity of their metal centers. Remarkably, the UiO-66-NH_2(Hf), with a stronger piezoelectric effect, demonstrated ≈2.2 times greater H_2 production activity than that of UiO-66-NH_2(Zr) when subjected to light and ultrasonic exposure. Zhao et al. prepared UiO-66(Zr)-F_4 for piezoelectric catalytic reaction,[30] where the introduction of highly polar fluorine ligands not only reduced the band gap of MOFs but also improved its piezoelectric properties. As a consequence, the piezoelectric hydrogen evolution rate of UiO-66(Zr)-F_4 significantly exceeded that of UiO-66(Zr). These findings indicate a strong correlation between polar characteristics of MOFs and their piezoelectric properties, while augmenting the polarity can enhance piezoelectric potential and improve the charge carrier separation. Currently, research on MOFs in piezo-photocatalysis is very limited, primarily focused on the introduction of polar metal centers in UiO series. Therefore, developing novel piezoelectric MOFs and universal strategy to enhance their piezoelectricity is of paramount importance for advancing their application of piezoelectric photocatalysis.

Building on the above findings, we first employed a dual modulation strategy, involving ligand functionalization and metal coordination, to endow the MOFs with greater polarity. The introduction of amino group (—NH_2) reduced the band gap while strengthening its polarity resulting in improved piezoelectric photocatalytic activity. The performance is further improved when Cu ions is coordinated with the amino group. This dual modulation strategy greatly increased the polarity of the MOFs, resulting in a stronger piezoelectric effect, as confirmed by a wealth of evidence, such as in situ Raman tests, DFT calculations of dipole moment, and COMSOL simulations. As a result, under the synergistic effect of ultrasound and light, the hydrogen production rate of Cu-NH_2-MIL-125 reaches up to ≈2884.20 $\mu mol \cdot g^{-1} \cdot h^{-1}$, which is ≈2.76 and 9.92 times higher than that of NH_2-MIL-125 and MIL-125, respectively. Our finding underscores the promising potential of utilizing built-in polarity as driving forces to tackle severe carrier recombination in MOFs.

2. Results and Discussion

The synthetic route for Cu-modified NH_2-MIL-125 is illustrated in **Figure 1a**. In the initial step, the NH_2-MIL-125 catalyst is prepared via a straightforward solvothermal approach (150 °C, 8 h) employing 2-amino-1,4-phthalic acid (NH_2-BDC) and titanium isopropoxide as raw materials. Subsequently, the Cu-NH_2-MIL-125 catalyst with a further incorporation of Cu ions is acquired by the post-synthetic method through immersing the NH_2-MIL-125 samples in an ethanol solution of copper salts for 8 h.[31] Furthermore, to demonstrate the important role of amino group (—NH_2), the classical MIL-125 MOFs has also been synthesized based on previous work.[32]

As shown in the scanning electron microscopy (SEM) images in Figure 1b,c and Figure S1 (Supporting Information), all the samples (MIL-125, NH_2-MIL-125, and Cu-NH_2-MIL-125) exhibit a similar disk-like morphology with nanometer-scale dimensions, which is also confirmed by transmission electron microscopy (TEM) images in Figure S2 (Supporting Information). The energy dispersive spectrometer (EDS) element mapping images in Figure 1d reveal a uniform distribution of C, N, O, Ti, and Cu over the surface of Cu-NH_2-MIL-125, which confirms the successful decoration of Cu ions on NH_2-MIL-125.

Simultaneously, to demonstrate the universality of our strategy and study the effects of different transition metal centers on the performance, cobalt (Co) and nickel (Ni) are also incorporated into the NH_2-MIL-125, following the same approach as for Cu-NH_2-MIL-125. These samples are designated as Co-NH_2-MIL-125 and Ni-NH_2-MIL-125, with the corresponding TEM and EDS images shown in Figures S3–S5 (Supporting Information).

The powder X-ray diffraction (PXRD) patterns of NH_2-MIL-125 and Cu-NH_2-MIL-125 are found to be identical to that of MIL-125, and all of them are consistent with the standard card (CCDC 751157) (Figures S6–S8, Supporting Information).[33] The results not only corroborate the isostructural nature of the three metal–organic frameworks, but also confirm the preservation of the NH_2-MIL-125's crystalline structure following the introduction of copper ions. The thermal stability of samples is investigated

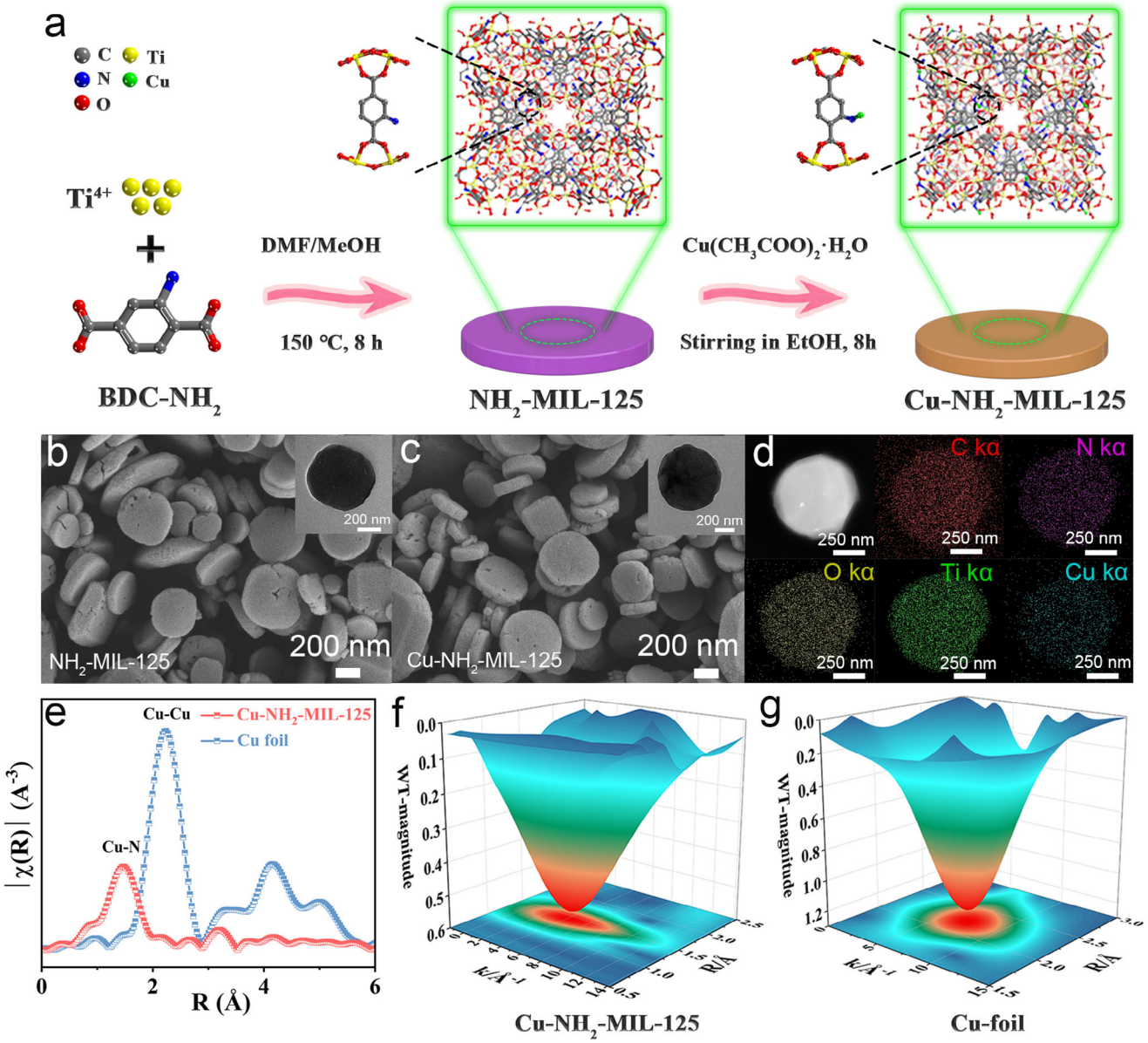

Figure 1. a) The schematic diagram of the synthesis of NH_2-MIL-125 and Cu-NH_2-MIL-125. b,c) SEM images of NH_2-MIL-125 and Cu-NH_2-MIL-125. The inserts are their TEM images. d) EDS elemental mapping images of Cu-NH_2-MIL-125. e) Fourier transformed (FT) k^2-weighted EXAFS of the Cu K-edge of Cu-NH_2-MIL-125. The data is not phase-corrected. f,g) Wavelet transformed (WT) EXAFS of Cu-NH_2-MIL-125 and Cu-foil samples.

using thermogravimetric analysis (TGA), as displayed in Figure S9 (Supporting Information), which reveals a two-stage weight loss. The initial weight loss stage from 60 to 200 °C is due to the release of solvent molecules confined within the pores, while the subsequent stage, occurring from 350 to 800 °C, is attributed to the structural collapse of MOFs. The permanent porosity of the samples is further analyzed through N_2 adsorption/desorption measurements at 77 K. As shown in Figure S10 (Supporting Information), both NH_2-MIL-125 and Cu-NH_2-MIL-125 display fully reversible type-I isotherms with a characterization of microporosity, with BET surface area (S_{BET}) calculated as 1239.30 and 1069.70 $m^2 \cdot g^{-1}$, respectively (Table S1, Supporting Information). The decrease in S_{BET} of Cu-NH_2-MIL-125 can be attributed to the coordination of Cu ions on NH_2-MIL-125, which results in partial blockage of the pores in the NH_2-MIL-125 framework. In addition, the pore size distribution of the synthesized catalysts is presented in Figures S11 and S12 (Supporting Information). The pore volumes of NH_2-MIL-125 and Cu-NH_2-MIL-125 are ≈0.54 and 0.48 $cm^3 \cdot g^{-1}$ and the average pore diameters are ≈2.51 and 2.47 nm, respectively.

Fourier transform infrared spectroscopy (FT-IR) results indicate that compared to MIL-125, both NH_2-MIL-125 and Cu-NH_2-MIL-125 show a discernible shift in absorption peak positions, accompanied by a slight decrease in peak intensity (Figure S13, Supporting Information). This change can be ascribed to the pronounced impact of coordination interactions between Cu ions

and —NH_2 groups.[31] Additionally, Raman spectroscopy results in Figure S14 (Supporting Information) reveal that the NH_2-MIL-125 exhibits additional peaks beyond those characteristics of the material MIL-125. Specifically, compared to the spectrum of MIL-125, the presence of an additional absorption peak at ≈1586 cm^{-1} for NH_2-MIL-125 is associated with N—H bending mode of the —NH_2 functional group. The wagging or twisting vibrational modes of the —NH_2 group are also clearly observed in the region from 1200 to 1300 cm^{-1}. These observations corroborate the successful incorporation of —NH_2 moieties within the NH_2-MIL-125.[6] Notably, for the Cu-NH_2-MIL-125, there is a distinct change in both the intensity and position of all the peaks. Particularly, the peak observed at ≈1583 cm^{-1} in the Cu-NH_2-MIL-125 correlates with the stretching vibrations of the —NH_2 moieties, which are perturbed by the coordination of Cu ions as expected.

The chemical composition and surface electronic states of these samples are studied by X-ray photoelectron spectroscopy (XPS) analysis. The XPS survey spectra confirm that NH_2-MIL-125 includes C, N, O, and Ti elements, while Cu-NH_2-MIL-125 contains C, N, O, Ti, and Cu elements (Figure S15, Supporting Information). The Ti 2p spectrum exhibits a pair of binding energy peaks at 458.9 and 464.7 eV, corresponding to $2p_{3/2}$ and $2p_{1/2}$ of Ti^{4+} in NH_2-MIL-125, respectively (Figure S16, Supporting Information). Besides, compared with NH_2-MIL-125, the XPS spectrum of Ti for Cu-NH_2-MIL-125 displays a slight downshift, indicate a change in the electronic environment.[7] In the N 1s XPS of NH_2-MIL-125, the peak at ≈402.3 eV is attributed to the positively charged nitrogen species, while the peak at 399.6 eV corresponds to the —NH_2. However, in Cu-NH_2-MIL-125, these two peaks are shifted due to the localized electron distribution of the —NH_2 group (Figure S17, Supporting Information).[34] Additionally, the Cu $2p_{3/2}$ peak observed at 935.1 eV in Figure S18 (Supporting Information), accompanied by shake-up lines ≈943.6 eV, is identified as Cu^{2+} within Cu-NH_2-MIL-125. It also has a more predominant peak at 932.8 eV which corresponds to Cu^{+}. These collective results unequivocally demonstrate the coexistence of both +1 and +2 oxidation states of Cu within the Cu-NH_2-MIL-125.[31] The extended X-ray absorption spectroscopy fine structure (EXAFS) of the Cu K-edge is also examined to investigate geometrical structure of Cu-NH_2-MIL-125 at atomic level. The Fourier transform (FT) curve of Cu K-edge EXAFS in Figure 1e of Cu-NH_2-MIL-125 displays a dominating peak at ≈1.5 Å, which corresponds to the scattering paths associated with Cu—N bonds. No peak corresponding to Cu—Cu (≈2.2 Å) is observed in Cu-NH_2-MIL-125 as that observed in Cu foil.[31] Additionally, wavelet transforms (WT) of Cu K-edge EXAFS shown in Figure 1f also confirm the existence of Cu—N coordination bond in the Cu-NH_2-MIL-125. Therefore, these consistent results of XPS and EXAFS collectively substantiate the formation of a chemical coordination bond between —NH_2 groups and Cu ions. Moreover, the WT-EXAFS and the FT-EXAFS curves for Ni-NH_2-MIL-125 and Co-NH_2-MIL-125 also demonstrate the presence of Co—N and Ni—N bonds (Figures S19–S22, Supporting Information).

The incorporation of —NH_2 groups and Cu ions may have significant impact for the polarity of the MOFs, thus affecting their charge transfer and photocatalytic performance. To validate our hypothesis, series control tests, including photocatalytic, piezo-catalytic, and piezo-photocatalytic H_2 evolution reactions, have also been investigated. As shown in **Figure 2a**, the Cu-NH_2-MIL-125 catalyst achieves an extremely high photocatalytic H_2 production rate of 651.81 $\mu mol \cdot g^{-1} \cdot h^{-1}$ under light irradiation, which is ≈4.81 or 2.10 times higher than that of MIL-125 (135.52 $\mu mol \cdot g^{-1} \cdot h^{-1}$) and NH_2-MIL-125 (310.49 $\mu mol \cdot g^{-1} \cdot h^{-1}$) catalysts. It is worth mentioning that with the incorporation of piezoelectric catalytic technology, the catalytic activity of Cu-NH_2-MIL-125 under both light and ultrasonic radiation is further enhanced to 2884.20 $\mu mol \cdot g^{-1} \cdot h^{-1}$, which is 2.76 and 9.92 times higher than that of NH_2-MIL-125 (1044.51 $\mu mol \cdot g^{-1} \cdot h^{-1}$) and MIL-125 (290.60 $\mu mol \cdot g^{-1} \cdot h^{-1}$), respectively. This performance has surpassed most of the state-of-the-art piezo-photocatalytic materials previously reported (Figure 2i; Table S3, Supporting Information). To explore the role of polarity in the piezo-photocatalysis and its dependence on the vibration force, the natural frequency (f) of Cu-NH_2-MIL-125 is calculated to be ≈48.39 kHz. This value is derived from the Young's modulus (E) and Equation S1 (Supporting Information), which is ≈8.55 GPa (Figure 2b). As shown in Figure 2c, Cu-NH_2-MIL-125 achieves the highest H_2 production rate at 50 kHz compared to that of 25 kHz and 75 kHz. This result suggests that optimizing the applied frequency to match well with the resonant frequency of catalyst materials is essential for maximizing carriers' participation in the water-splitting reaction.

Apart from vibration frequency, the vibration intensity is also an important factor for influencing their piezo-photocatalytic activity. As demonstrated in Figure 2d, the piezo-photocatalytic H_2 production rates over Cu-NH_2-MIL-125 progressively increases with the enhancement of applied ultrasound power. This trend can be attributed to the fact that a higher ultrasonic power provides a greater mechanical force exerted on the piezo-photocatalysts, thereby inducing a stronger piezoelectric potential to reduce the recombination rates of photo-generated carriers. The effects of various sacrificial agents on the piezo-photocatalytic H_2 production performance of the materials are also investigated. Figure 2e clearly demonstrates that the Cu-NH_2-MIL-125 exhibits the highest piezo-photocatalytic H_2 production activity when triethanolamine (TEOA) is utilized to consume the photo-generated holes, surpassing the performance achieved with other sacrificial agents. Additionally, the effectiveness of Cu-NH_2-MIL-125 in generating H_2 from various water matrices is also examined. As shown in Figure 2f, Cu-NH_2-MIL-125 demonstrates good piezo-photocatalytic H_2 production performance across various water sources, but it performs best in a deionized water system, outperforming both seawater and tap water systems. This finding suggests that impurities or ions present in seawater and tap water may have a negative impact on the catalytic performance of Cu-NH_2-MIL-125, as these substances can interfere with the active sites on the catalyst surface.[35]

The stability of the catalyst is also thoroughly investigated. Upon undergoing four cycles in deionized water, Cu-NH_2-MIL-125 exhibits only a slightly decline in its performance as demonstrated in Figure 2g. Both the XRD pattern and SEM images of Cu-NH_2-MIL-125 after the piezo-photocatalytic reactions confirm the commendable recyclability as shown in Figures S26 and S27 (Supporting Information). Additionally, Figure 2h shows that Co-NH_2-MIL-125 and Ni-NH_2-MIL-125 achieve a piezo-photocatalytic H_2 production rates of 1577.51 and

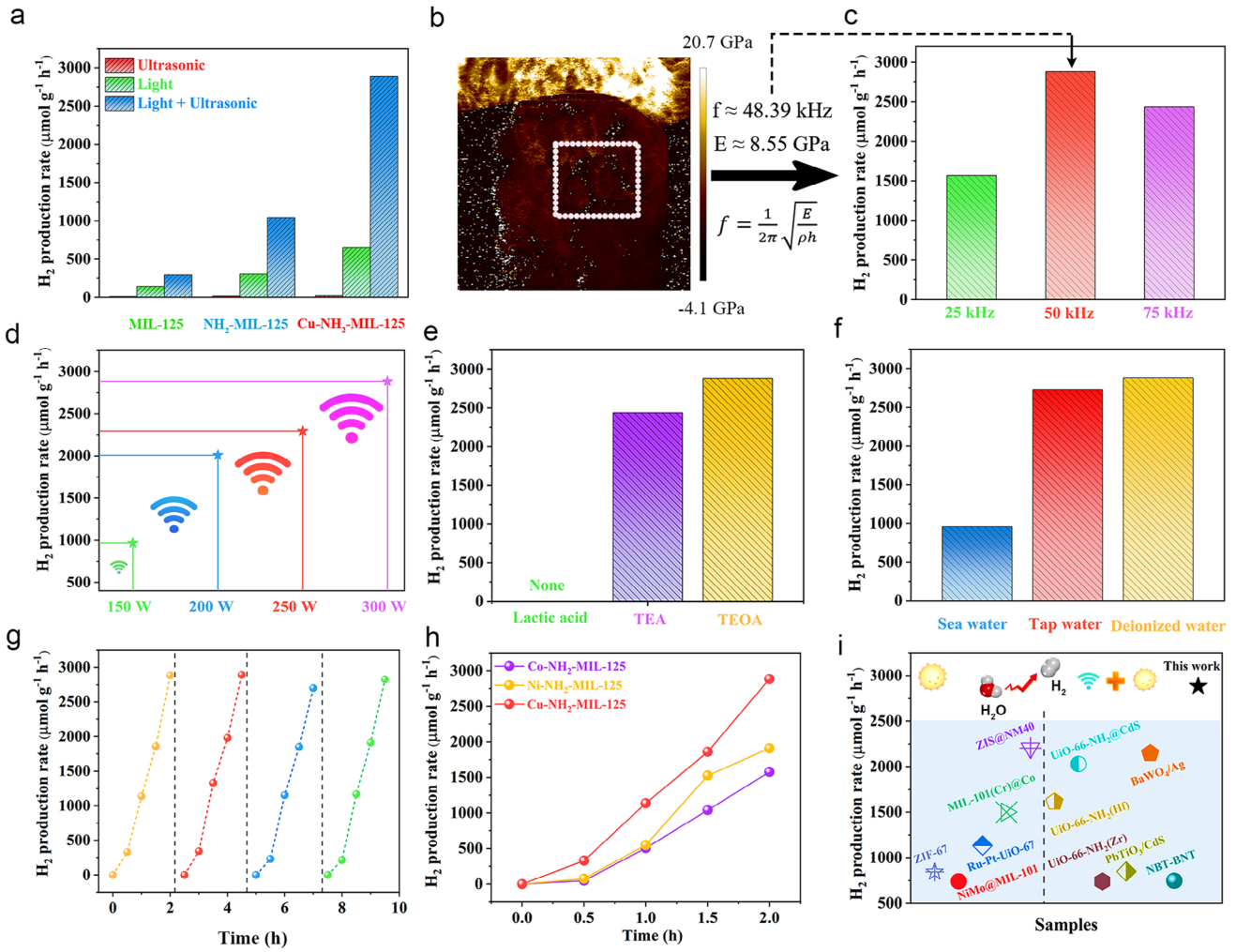

Figure 2. a) H_2 production rates of photo-catalysis, piezo-catalysis, and piezo-photocatalysis for MIL-125, NH_2-MIL-125, and Cu-NH_2-MIL-125. b) The Young's modulus test for Cu-NH_2-MIL-125. c) H_2 production rates of piezo-photocatalysis for Cu-NH_2-MIL-125 under different frequences. d) H_2 production rates of piezo-photocatalysis for Cu-NH_2-MIL-125 under different powers. e) Piezo-photocatalytic activity of Cu-NH_2-MIL-125 in different sacrificial agents. f) H_2 production rates of piezo-photocatalysis for Cu-NH_2-MIL-125 under different water matrices. g) Cyclic stability of H_2 production rates of piezo-photocatalysis for Cu-NH_2-MIL-125. h) H_2 production rates of piezo-photocatalysis for Co-NH_2-MIL-125, Ni-NH_2-MIL-125 and Cu-NH_2-MIL-125. i) Performance comparison of piezo-photocatalytic H_2 production rates behavior over Cu-NH_2-MIL-125 with state-of-the-art photocatalysts and piezo-photocatalysts in previous reports.

1909.80 μmol·g^{-1}·h^{-1} under the same experimental conditions, respectively. Overall, the successful incorporation of transient metal centers onto the piezo-photocatalyst material demonstrate significant potential for enhancing H_2 production through piezo-photocatalysis.

To validate that the enhancement in catalytic activity originates from the augmentation of piezoelectricity, a thorough investigation of the piezoelectric properties of three MOFs is carried out through the utilization of piezo-response force microscopy (PFM) (Figure S28, Supporting Information). The presence of piezoelectricity in MIL-125, NH_2-MIL-125, and Cu-NH_2-MIL-125 is confirmed by the characteristic butterfly-shaped amplitude and phase hysteresis loops observed when the material is subjected to a reversing electric field ranging from −8 to +8 V (**Figure 3**a; Figures S29–S31, Supporting Information). Cu-NH_2-MIL-125 exhibits a significant piezoelectric capability, with a maximum amplitude of ≈186.2 pm. While subjecting the material to a voltage loop from −8 to +8 V induces an almost 180° alteration in domain vector inversion. The d_{33} value of MIL-125, NH_2-MIL-125, and Cu-NH_2-MIL-125 are calculated to be ≈1.69, 11.75, and 26.21 pm/V, respectively, as calculated using Equation S2 (Supporting Information). This indicates that Cu-NH_2-MIL-125 has a significantly higher d_{33}, which have contributed greatly in efficiently transforming mechanical energy into chemical energy during the piezo-photocatalysis tests.[36] Furthermore, the phase retardation loop of Cu-NH_2-MIL-125 exhibits the narrowest width in comparison to its counterparts (MIL-125 and NH_2-MIL-125). This observation indicates that the Cu-NH_2-MIL-125 is capable of accomplishing efficient domain reorientation at a comparatively reduced voltage threshold compared to MIL-125 and NH_2-MIL-125, leading to an enhanced amplitude response.[20] All of above results demonstrate that the incorporation of Cu ions

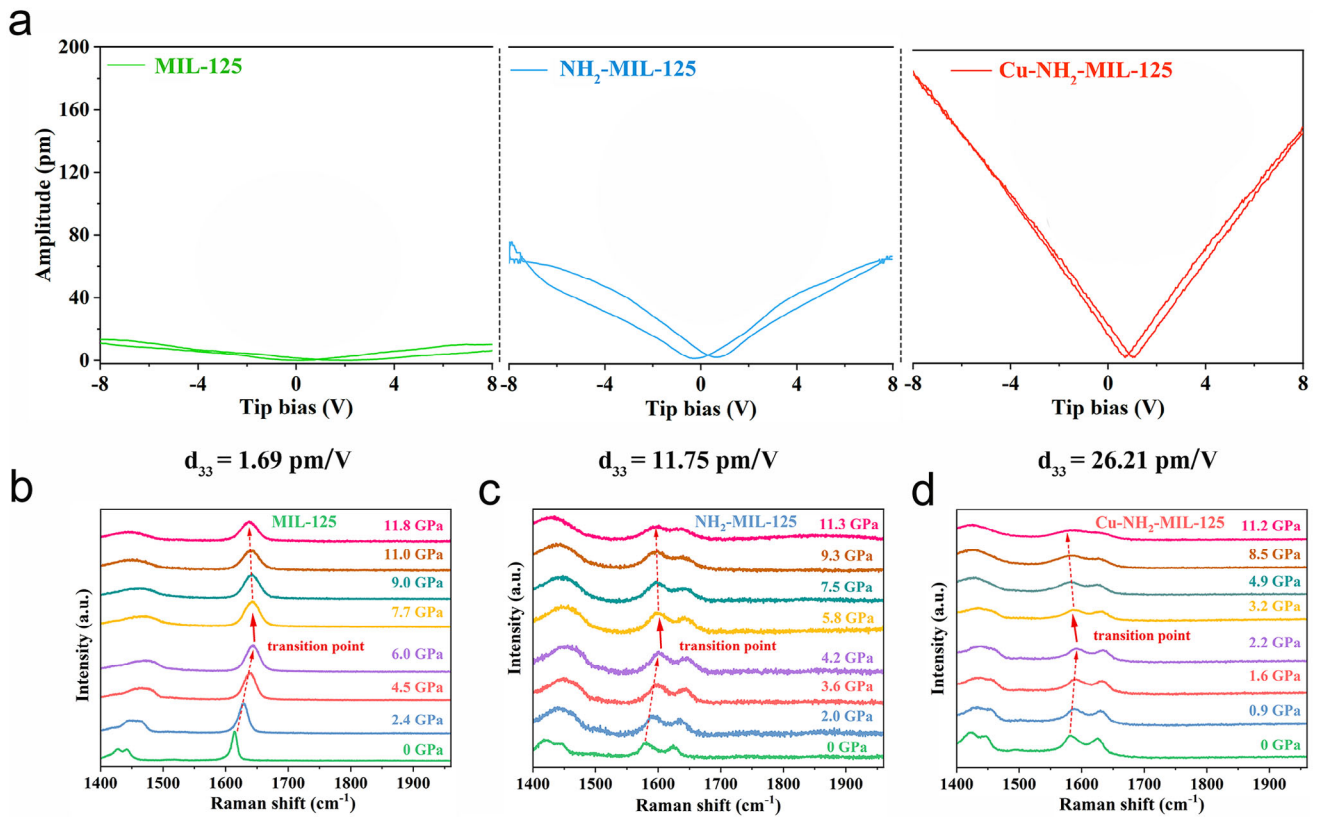

Figure 3. a) Butterfly-shaped amplitude curve of MIL-125, NH_2-MIL-125, and Cu-NH_2-MIL-125. b–d) In-situ Raman spectra of MIL-125, NH_2-MIL-125, and Cu-NH_2-MIL-125 upon different pressure at room temperature. Arrows reveal the moving trend of the peaks.

and —NH_2 groups into MOFs can significantly enhance its intrinsic piezoelectricity.

Moreover, the in situ Raman spectroscopy is employed to further reveal the underlying mechanism for the enhanced piezoelectricity for Cu-NH_2-MIL-125. As demonstrated in Figure 3b–d, with the increase of applied pressure, the Raman signals initially shift toward higher frequencies without any changes in the spectral distribution. Subsequently, the signals move toward lower frequencies. The transition pressure for MIL-125, NH_2-MIL-125, and Cu-NH_2-MIL-125 is determined to be 6.0, 4.2, and 2.2 GPa, respectively, which implies that the applied pressure induces structural phase transition in MIL-125, NH_2-MIL-125, and Cu-NH_2-MIL-125, resulting in the emergence of piezoelectric characteristics. Notably, Cu-NH_2-MIL-125 exhibits the lowest transition pressure among the three materials, underscoring its superior piezoelectric properties.[37] Furthermore, different mechanical forces (stirring and ultrasound) are employed to piezodeposit Ag on the surface of Cu-NH_2-MIL-125 in order to further validate the piezoelectricity of materials (Figure S32, Supporting Information). SEM images clearly illustrate that the number of Ag nanoparticles deposited on the surface of Cu-NH_2-MIL-125 is significantly greater when using ultrasonic vibration as the mechanical force source than those achieved through stirring. This observation serves as additional evidence supporting the intrinsic piezoelectric characteristics of Cu-NH_2-MIL-125, while different mechanical forces can have different effects on the piezoelectric catalytic performance.

Previous studies have proven that the piezoelectricity of MOFs is closely linked to their polarity. Density functional theory (DFT) calculations, which is powerful in elucidating the changes in dipole moment resulting from the introduction of —NH_2 groups and Cu ions, are then employed to unveil the polarity difference and the reason for the enhanced piezoelectricity. The dipole moment, which arises from the non-coincidence of positively and negatively charged centers, is initially computed to be 6.60 D for MIL-125. Upon the incorporation of —NH_2, the dipole moment increases to 18.80 D, and it is further significantly enhanced to 25.99 D with the introduction of the Cu^{2+}/Cu^{+} center (**Figure 4a**). This substantial dipole moment signifies the potential for utilizing dipole field-driven polarization in Cu-NH_2-MIL-125 to facilitate photo-generated charge separation.[38]

As confirmed, the —NH_2 modification and Cu coordination enhances the polarity of the MOFs, resulting in a stronger piezoelectric field under mechanical force. To gain a deeper understanding of the relationship between the introduction of —NH_2, transition metal centers, and the piezoelectric potential of series MOFs, finite element method (FEM) analysis utilizing COMSOL Multiphysics software is conducted to simulate the distribution of piezoelectric potential on MIL-125, NH_2-MIL-125, and Cu-NH_2-MIL-125.[39] The FEM simulation for geometric model and meshing is illustrated in Figures S33 and S34 (Supporting Information). Based on the actual size observed in SEM images (Figure 1b,c), the simulated diameter (D) and thickness (T) are set at 600 × 100 nm^2. At the same time, a simulated force field is

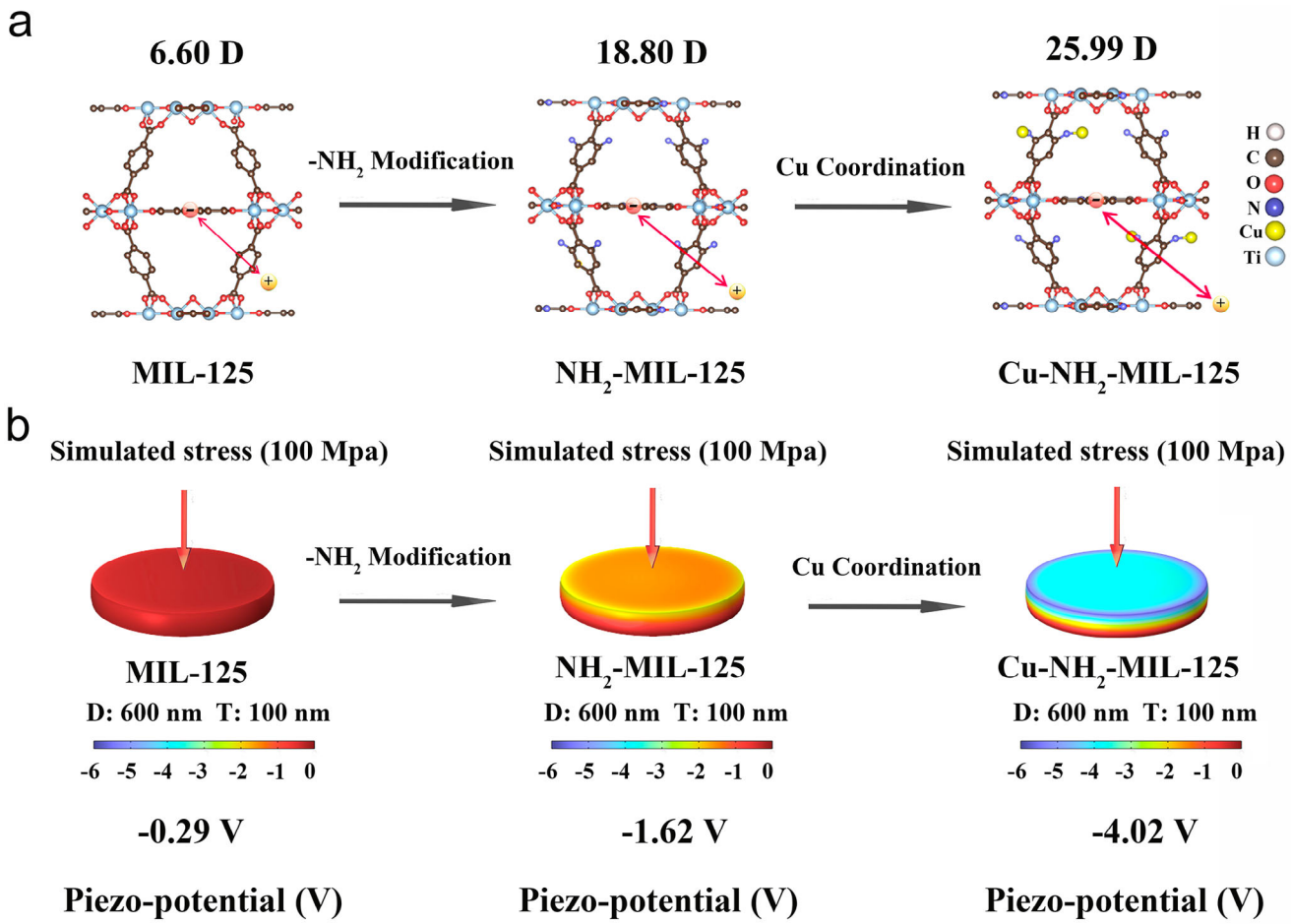

Figure 4. a) The simulated dipole moments of MIL-125, NH_2-MIL-125 and Cu-NH_2-MIL-125. b) The COMSOL simulated stress and potential distributions of prepared samples.

applied to exert a pressure of 100 MPa along the Z-axis, which is close to the force required to rupture cavitation bubbles. All materials experience deformation upon the simulated stress field, with Cu-NH_2-MIL-125 demonstrating an extremely larger piezoelectric potential difference of −4.02 V compared to the NH_2-MIL-125 (−1.62 V) and MIL-125 (−0.29 V), which is in concordance with the experimental data obtained (Figure 4b).

The introduction of $-NH_2$ groups and Cu ions not only increases the polarity of MOF materials to promotes carrier separation, but also affects their energy band structure, as revealed by the UV–vis diffuse reflectance spectroscopy (UV–vis–DRS). It is evident that the incorporation of $-NH_2$ and coordination of Cu ions cause a red shift in the maximum absorption wavelength (MAV) of MIL-125 (Figure S35, Supporting Information), which enhances the light-harvesting performance of the MOFs materials. Based on the Tauc plot and Equation S3 (Supporting Information), the direct optical band gap values of MIL-125, NH_2-MIL-125, and Cu-NH_2-MIL-125 are determined to be ≈3.65, 2.66, and 2.60 eV, respectively (Figures S36–S38, Supporting Information). From the Mott–Schottky (M—S) plots, the as-prepared materials exhibit a positive slope, indicating that they are n-type semiconductors (Figures S39–S41, Supporting Information). Besides, the flat band potential can also be directly obtained based on M—S plots (Equation S4, Supporting Information). Generally, in n-type semiconductors, the Fermi level tends to be ≈0.1–0.3 V higher than the lowest unoccupied molecular orbital (LUMO) level.[40] Consequently, the LUMO level for MIL-125, NH_2-MIL-125, and Cu-NH_2-MIL-125 are calculated as ≈−0.52, −0.60, and −0.91 V, respectively. As expected, these LUMO level are more negative compared to the potential of H^+/H_2 (−0.41 V versus NHE, pH = 7), indicating the capability of H_2 generation. According to the bandgap values obtained above, the highest occupied molecular orbital (HOMO) level can be obtained, which are ≈3.13, 2.06, and 1.69 V for MIL-125, NH_2-MIL-125, Cu-NH_2-MIL-125, respectively (Equation S5, Supporting Information). Therefore, it can be inferred that the energy band structures of the MIL-125, NH_2-MIL-125, and Cu-NH_2-MIL-125 catalysts are conducive to the reduction of H^+ to H_2, which is thermodynamically favorable for promoting water reduction. Similarly, the corresponding energy band structures of Co-NH_2-MIL-125 and Ni-NH_2-MIL-125 are also analyzed and demonstrated to be favorable for water reduction (Figures S42–S46, Supporting Information).

The performance of a material in piezo-photocatalysis is also associated with its ability to facilitate the effective separation and transfer of photo-generated carriers. As shown in Figure S47 (Supporting Information), the photoluminescence (PL)

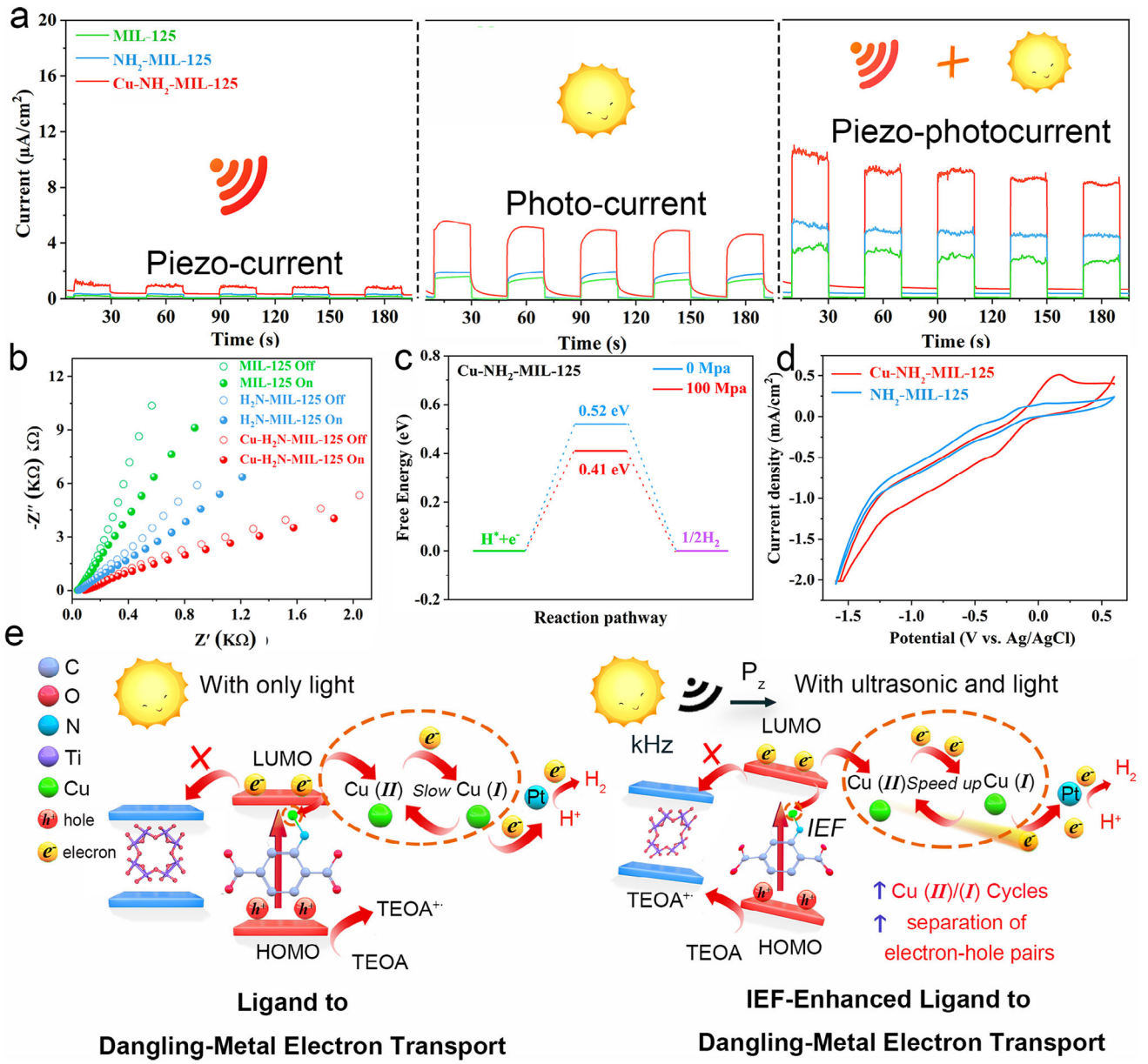

Figure 5. a) The current response for MIL-125, NH_2-MIL-125, and Cu-NH_2-MIL-125 under light irradiation, ultrasonic vibration, or ultrasonic vibration combined with light irradiation. b) EIS for prepared samples under or in the absence of ultrasonic vibration. c) ΔG_{H^*} diagram of Cu-NH_2-MIL-125 in the HER reaction process with and without pressure (100 MPa). d) The cyclic voltammograms (CV) tests for NH_2-MIL-125 and Cu-NH_2-MIL-125. e) The catalytic mechanism of Cu-NH_2-MIL-125.

intensity of Cu-NH_2-MIL-125 is found to be lower than that of MIL-125 and NH_2-MIL-125, indicating a significant reduced recombination rates of photo-generated charge carriers. To gain further insights into the transfer process of photo-generated carriers during the photocatalytic process, time-resolved photoluminescence (TR-PL) spectroscopy is applied (Figure S48, Supporting Information). The average emission lifetimes of MIL-125, NH_2-MIL-125, Cu-NH_2-MIL-125 are calculated to be ≈2.74, 3.62, and 3.92 ns (Equations S6 and S7, Supporting Information), respectively, as listed in Table S5 (Supporting Information). An increase in PL lifetime indicates a decrease in the recombination probability of photo-generated electron-hole pairs. The open circuit voltage decay (OCVD) images in Figures S49 and S50 (Supporting Information) allow us to determine the carrier lifespan, revealing that Cu-NH_2-MIL-125 has the longest carrier lifetime (Equation S8, Supporting Information). Furthermore, a linear sweep voltammetry (LSV) analysis reveals that Cu-NH_2-MIL-125 has a more favorable electrocatalytic onset potential for hydrogen evolution, outperforming both MIL-125 and NH_2-MIL-125 under equivalent current density conditions (Figure S51, Supporting Information). The CV curves in **Figure 5**d indicates that Cu-NH_2-MIL-125 features two reversible redox peaks at ≈−0.32 and 0.16 V, which is associated with a reversible Cu^{2+}/Cu^{+} redox process. This result, along with the photo-electric

measurements, suggests that incorporating transient Cu^{2+}/Cu^{+} centers into NH_2-MIL-125 is an effective solution to alleviate the recombination of photo-generated carriers.

To further demonstrate the significant contribution of polarity in promoting the charge carrier separation/migration, the transient current response of the materials with on-off cycles of ultrasound vibration, simulate sunlight irradiation, and ultrasound vibration-simulate sunlight irradiation condition are studied separately. As depicted in Figure 5a, the Cu-NH_2-MIL-125 sample exhibits the highest piezo-photocurrent and photocurrent response when either subjected to ultrasonic vibration or simulate sunlight irradiation. This enhancement suggests that the Cu-NH_2-MIL-125 sample is more effective at suppressing carrier recombination compared to the MIL-125 and NH_2-MIL-125 samples. It is worth mentioning that the introduction of ultrasound vibration in the present of light irradiation leads to a further improvement in the current response of all materials, with Cu-NH_2-MIL-125 exhibiting the highest piezo-photocurrent intensity. This provides strong evidence that ultrasound vibration facilitates the separation of photo-generated carriers in the catalyst, allowing these carriers to effectively drive the piezo-photocatalytic H_2 production reaction. Besides, the photocurrent response of Co-NH_2-MIL-125 and Ni-NH_2-MIL-125 is also enhanced under ultrasound, further providing additional evidence supporting the broad applicability of our methodology (Figures S53 and S54, Supporting Information).

To further validate these results, electrochemical impedance spectroscopy (EIS) measurements are conducted to investigate the carrier transport properties. As depicted in Figure 5b, the application of ultrasound significantly reduces the charge transfer resistance of MIL-125, NH_2-MIL-125, and Cu-NH_2-MIL-125 compared to the measurements taken without ultrasound. In addition, Cu-NH_2-MIL-125 and NH_2-MIL-125 exhibits smaller charge transfer resistance than that of MIL-125, indicating that the introduction of $-NH_2$ and Cu ions increases the polarity of the MOFs material, which facilitates the formation of internal electric field (IEF) under ultrasound and promotes carrier separation. Furthermore, in order to further reveal the effect of pressure on photocatalytic H_2 production performance, the free energy of hydrogen adsorption (ΔG_{H^*}) are stimulated under both pressurized and unpressurized conditions (Figure 5c). At a pressure of 100 MPa, the ΔG_{H^*} value decreases from ≈0.52 to 0.41 eV for Cu-NH_2-MIL-125, indicating a reduced energy barrier for the adsorption of hydrogen.[41] This reduction suggests that the photocatalytic reaction becomes more favorable and efficient, leading to an enhanced rate of H_2 production. In addition, the water contact angle (WCA) measurements are conducted to investigate the surface wettability of the samples. As illustrated in Figures S56–S61 (Supporting Information), Cu-NH_2-MIL-125 presents the lowest contact angle, indicating that the Cu-NH_2-MIL-125 owns the highest hydrophobicity. This surface property enables the catalysts to establish full contact with water which is beneficial for the H_2 release.

Based on all above analyses, the mechanism of H_2 production from Cu-NH_2-MIL-125 by piezo-photocatalysis can be outlined as follows (Figure 5e). Upon exposure to light, the HOMO of organic linkers becomes active, inducing the generation of electrons at the LUMO level. These photo-generated electrons are then transferred from the linkers to the Cu (I&II) centers, rather than to the TiO_x clusters. This electron transfer initiates the transformation of Cu (II) centers into Cu (I) centers, resulting in an effective storage of energy. The electrons stored at the Cu (I) sites can be easily captured and then transferred to the co-catalyst Pt. This promotes the efficient reduction of H_2O while simultaneously converting Cu (I) back to Cu (II). Throughout this sequence, photo-generated holes within the HOMO of the organic linkers are subsequently consumed by TEOA. The NH_2-MIL-125 with transitional Cu centers significantly enhances the separation of photo-generated carriers through this alternative ligand-to-dangling metal electron transport (LDMET) process, rather than the traditional ligand-to-metal charge transfer (LMCT) process. Nonetheless, the extensive recombination of photo-generated carriers within the catalyst still limits the photocatalytic performance of Cu-NH_2-MIL-125. With the help of ultrasonic vibration, the tiny bubbles in liquid vibrate, grow, and continuously gather sound field energy under the action of ultrasonic waves. When the energy reaches a certain threshold, cavitation bubbles collapse rapidly, resulting in high local pressure exceeding 100 MPa. Combined with the acoustic pressure generated by the ultrasonic wave, the deformation of the piezo-catalyst is induced. In this case, polarized electric dipoles are formed in the catalyst to generate a piezoelectric field inside the MOFs. Upon simultaneous simulate light and ultrasonic irradiation, the photo-generated electrons and holes are driven by the internal piezoelectric potential to the opposite directions/sides. Both the HOMO and LUMO are tilted by this piezoelectric potential simultaneously. Notably, the larger piezoelectric potential in Cu-NH_2-MIL-125, in contrast to NH_2-MIL-125, facilitates a more efficient and rapid participation of photo-generated electrons in the cycles of Cu(II)/Cu(I). These electrons are then transferred to the Pt co-catalyst, where they then react with H^+ to form H_2. Therefore, the IEF caused by the piezoelectric effect greatly promotes the photocurrent transport, thereby improving the H_2 release activity. Consequently, the combination of piezoelectric and photocatalytic technologies result in exceptional catalytic efficiency in H_2 production.

3. Conclusion

In summary, this research demonstrates a novel possibility for enhancing the piezoelectricity of MOFs through the ligand functionalization and the metal incorporation, leading to an improved piezo-photocatalytic performance. The Cu-NH_2-MIL-125 demonstrated an impressive piezo-photocatalytic H_2 production rate (2884.20 $\mu mol \cdot g^{-1} \cdot h^{-1}$), which is 2.76 times higher than that of NH_2-MIL-125 (1044.51 $\mu mol \cdot g^{-1} \cdot h^{-1}$) and 9.92 times as high as that of MIL-125 (290.6 $\mu mol \cdot g^{-1} \cdot h^{-1}$) at the same reaction condition. The enhanced performance originates from the synergistic effect between NH_2-MIL-125 and Cu ions, yielding an expanded range of responsiveness to light due to the d-d transition band of Cu, as well as a stronger piezoelectric field caused by piezoelectric polarization charges. While the broader visible light response range facilitates increased participation of photo-generated carriers in the reaction, the established piezoelectric field simultaneously drives the efficient separation of these carriers. This process also governs carrier movement within the space charge region to enhance the reversible reduction-oxidation of Cu(II)/Cu(I) centers, ultimately achieving a remarkable synergy between

piezo-catalysis and photocatalysis. The presented work offers a viable and effective approach for developing high-performance MOFs-based piezo-photocatalysts through a dual polarity modulation strategy.

Supporting Information

Supporting Information is available from the Wiley Online Library or from the author.

Acknowledgements

H.H., and X.L. contributed equally to this work. This work was supported by the National Natural Science Foundation of China (Nos. 22101105, 22401198, 52071171, and 52202248), Liaoning Province Centrally Guided Local Science and Technology Development Fund Program (2024JH6/100700010, 2024JH6/100700011). Open Project of State Key Laboratory of Inorganic Synthesis and Preparative Chemistry (2024-35), Open Research Fund of Guangdong Advanced Carbon Materials Co., Ltd (Kargen-2024B1001). T.M. acknowledged the Australian Research Council (ARC) through Future Fellowship (FT210100298), Discovery Project (DP220100603), Linkage Project (LP210200504, LP220100088, LP230200897) and Industrial Transformation Research Hub (IH240100009) schemes, the Australian Government through the Cooperative Research Centers Projects (CRCPXIII000077), the Australian Renewable Energy Agency (ARENA) as part of ARENA's Transformative Research Accelerating Commercialization Program (TM021), and European Commission's Australia-Spain Network for Innovation and Research Excellence (AuSpire). X.L. acknowledged the support of ARC DECRA fellowship (DE250100232). The authors thank Shiyanjia Lab (www.shiyanjia.com) for the support of TR-PL tests. The authors also thank SCI-GO (www.sci-go.com) for the support in the XPS tests. The authors also thank ZHONG KE BAI CE (www.zkbaice.cn) for XRD experiments.

Open access publishing facilitated by RMIT University, as part of the Wiley - RMIT University agreement via the Council of Australian University Librarians.

Conflict of Interest

The authors declare no conflict of interest.

Data Availability Statement

The data that support the findings of this study are available from the corresponding author upon reasonable request.

Keywords

hydrogen production, metal–organic frameworks, piezo-photocatalysis, polarity

Received: December 5, 2024
Revised: February 19, 2025
Published online: March 30, 2025

[1] W. Weng, J. Guo, *Nat. Commun.* **2022**, *13*, 5768.
[2] L. Feng, K.-Y. Wang, G. S. Day, M. R. Ryder, H.-C. Zhou, *Chem. Rev.* **2020**, *120*, 13087.
[3] A. Dhakshinamoorthy, Z. Li, S. Yang, H. Garcia, *Chem. Soc. Rev.* **2024**, *53*, 3002.
[4] S. Xie, Z. Zhou, X. Zhang, J. Fransaer, *Chem. Soc. Rev.* **2023**, *52*, 4292.
[5] S. Naghdi, A. Cherevan, A. Giesriegl, R. Guillet-Nicolas, S. Biswas, T. Gupta, J. Wang, T. Haunold, B. C. Bayer, G. Rupprechter, M. C. Toroker, F. Kleitz, D. Eder, *Nat. Commun.* **2022**, *13*, 282.
[6] C. Zhang, C. Xie, Y. Gao, X. Tao, C. Ding, F. Fan, H.-L. Jiang, *Angew. Chem., Int. Ed.* **2022**, *61*, 202204108.
[7] L. Liu, S. Du, X. Guo, Y. Xiao, Z. Yin, N. Yang, Y. Bao, X. Zhu, S. Jin, Z. Feng, F. Zhang, *J. Am. Chem. Soc.* **2022**, *144*, 2747.
[8] N.-Y. Huang, Y.-T. Zheng, D. Chen, Z.-Y. Chen, C.-Z. Huang, Q. Xu, *Chem. Soc. Rev.* **2023**, *52*, 7949.
[9] X. Li, K. Chen, R. Guo, Z. Wei, *Chem. Rev.* **2023**, *123*, 10432.
[10] S. Navalón, A. Dhakshinamoorthy, M. Álvaro, B. Ferrer, H. García, *Chem. Rev.* **2023**, *123*, 445.
[11] Y.-L. Li, A.-J. Li, S.-L. Huang, J. J. Vittal, G.-Y. Yang, *Chem. Soc. Rev.* **2023**, *52*, 4725.
[12] Y. Liang, E. Li, K. Wang, Z.-J. Guan, H.-h. He, L. Zhang, H.-C. Zhou, F. Huang, Y. Fang, *Chem. Soc. Rev.* **2022**, *51*, 8378.
[13] Q. Mo, L. Zhang, S. Li, H. Song, Y. Fan, C.-Y. Su, *J. Am. Chem. Soc.* **2022**, *144*, 22747.
[14] H. Wang, X. Zhang, W. Zhang, M. Zhou, H.-L. Jiang, *Angew. Chem., Int. Ed.* **2024**, *63*, 202401443.
[15] S.-Y. Han, D.-L. Pan, H. Chen, X.-B. Bu, Y.-X. Gao, H. Gao, Y. Tian, G.-S. Li, G. Wang, S.-L. Cao, C.-Q. Wan, G.-C. Guo, *Angew. Chem., Int. Ed.* **2018**, *57*, 9864.
[16] X. Ma, L. Wang, Q. Zhang, H.-L. Jiang, *Angew. Chem., Int. Ed.* **2019**, *58*, 12175.
[17] L. Yuan, C. Zhang, Y. Zou, T. Bao, J. Wang, C. Tang, A. Du, C. Yu, C. Liu, *Adv. Funct. Mater.* **2023**, *33*, 2214627.
[18] S. Tu, Y. Guo, Y. Zhang, C. Hu, T. Zhang, T. Ma, H. Huang, *Adv. Funct. Mater.* **2020**, *30*, 2005158.
[19] W. Amdouni, M. Fricaudet, M. Otoničar, V. Garcia, S. Fusil, J. Kreisel, H. Maghraoui-Meherzi, B. Dkhil, *Adv. Mater.* **2023**, *35*, 2301841.
[20] J. Yuan, W. Feng, Y. Zhang, J. Xiao, X. Zhang, Y. Wu, W. Ni, H. Huang, W. Dai, *Adv. Mater.* **2024**, *36*, 2303845.
[21] Y. Wang, X. Li, Y. Chen, Y. Li, Z. Liu, C. Fang, T. Wu, H. Niu, Y. Li, W. Sun, W. Tang, W. Xia, K. Song, H. Liu, W. Zhou, *Adv. Mater.* **2023**, *35*, 2305257.
[22] W. Liu, P. Wang, Y. Ao, J. Chen, X. Gao, B. Jia, T. Ma, *Adv. Mater.* **2022**, *34*, 2202508.
[23] Z.-Z. Liang, X.-A. Li, Q.-Z. Chen, X.-L. Wang, P.-Y. Su, J.-F. Huang, Y. Zhou, L.-M. Xiao, J.-M. Liu, *ACS Catal.* **2024**, *14*, 10447.
[24] H.-P. Lv, Y.-R. Li, X.-J. Song, N. Zhang, R.-G. Xiong, H.-Y. Zhang, *J. Am. Chem. Soc.* **2023**, *145*, 3187.
[25] L. Liu, M. Ruan, C. Wang, Z. Liu, *Appl. Catal. B: Environ.* **2024**, *354*, 124117.
[26] C. Wang, C. Hu, F. Chen, H. Li, Y. Zhang, T. Ma, H. Huang, *Adv. Funct. Mater.* **2023**, *33*, 2301144.
[27] C. Yu, J. He, M. Tan, Y. Hou, H. Zeng, C. Liu, H. Meng, Y. Su, L. Qiao, T. Lookman, Y. Bai, *Adv. Funct. Mater.* **2022**, *32*, 2209365.
[28] B. Dai, G. M. Biesold, M. Zhang, H. Zou, Y. Ding, Z. L. Wang, Z. Lin, *Chem. Soc. Rev.* **2021**, *50*, 13646.
[29] C. Zhang, D. Lei, C. Xie, X. Hang, C. He, H.-L. Jiang, *Adv. Mater.* **2021**, *33*, 2106308.
[30] S. Zhao, M. Liu, Y. Zhang, Z. Zhao, Q. Zhang, Z. Mu, Y. Long, Y. Jiang, Y. Liu, J. Zhang, S. Li, X. Zhang, Z. Zhang, *Mater. Horiz.* **2022**, *9*, 1978.
[31] X. Chen, S. Xiao, H. Wang, W. Wang, Y. Cai, G. Li, M. Qiao, J. Zhu, H. Li, D. Zhang, Y. Lu, *Angew. Chem., Int. Ed.* **2020**, *59*, 17182.
[32] Y. Fu, D. Sun, Y. Chen, R. Huang, Z. Ding, X. Fu, Z. Li, *Angew. Chem., Int. Ed.* **2012**, *51*, 3364.
[33] M. Dan-Hardi, C. Serre, T. Frot, L. Rozes, G. Maurin, C. Sanchez, G. Férey, *J. Am. Chem. Soc.* **2009**, *131*, 10857.

[34] G. Wang, Y. Wu, Z. Li, Z. Lou, Q. Chen, Y. Li, D. Wang, J. Mao, *Angew. Chem., Int. Ed.* **2023**, *62*, 202218460.
[35] Y. Li, H. Zhou, S. Cai, D. Prabhakaran, W. Niu, A. Large, G. Held, R. A. Taylor, X.-P. Wu, S. C. E. Tsang, *Nat. Catal.* **2024**, *7*, 77.
[36] R. Su, Z. Wang, L. Zhu, Y. Pan, D. Zhang, H. Wen, Z.-D. Luo, L. Li, F.-t. Li, M. Wu, L. He, P. Sharma, J. Seidel, *Angew. Chem., Int. Ed.* **2021**, *60*, 16019.
[37] P. Zhang, D. Gao, X. Tang, X. Yang, H. Zheng, Y. Wang, X. Wang, J. Xu, Z. Wang, J. Liu, X. Wang, J. Ju, M. Tang, X. Dong, K. Li, H.-k. Mao, *J. Am. Chem. Soc.* **2023**, *145*, 6845.
[38] Z. Li, Y. Zhou, Y. Zhou, K. Wang, Y. Yun, S. Chen, W. Jiao, L. Chen, B. Zou, M. Zhu, *Nat. Commun.* **2023**, *14*, 5742.
[39] Y. Zhang, M. Wu, Q. Zhu, F. Wang, H. Su, H. Li, C. Diao, H. Zheng, Y. Wu, Z. L. Wang, *Adv. Funct. Mater.* **2019**, *29*, 1904259.
[40] S. Wang, Z. Ai, X. Niu, W. Yang, R. Kang, Z. Lin, A. Waseem, L. Jiao, H.-L. Jiang, *Adv. Mater.* **2023**, *35*, 2302512.
[41] M.-L. Xu, M. Lu, G.-Y. Qin, X.-M. Wu, T. Yu, L.-N. Zhang, K. Li, X. Cheng, Y.-Q. Lan, *Angew. Chem., Int. Ed.* **2022**, *61*, 202210700.